JOURNAL OF MATERIALS SCIENCE 27 (1992) 839–852

Fabrication and characterization of some novel reaction-bonded silicon carbide materials

A. J. WHITEHEAD, T. F. PAGE
Materials Division, Department of Mechanical, Materials and Manufacturing Engineering, The University, Newcastle upon Tyne NE1 7RU, UK

Attempts have been made to produce modified reaction-bonded silicon carbide (RBSC) ceramics by incorporating a dispersion of other phases into the initial powder mix. ZrC, TiC, TaC and B_4C were chosen as additives together with TiB_2 as a phase likely to produce microcrack toughening in the final compact. During fabrication an important factor appears to be the possible reactions of the added phase with liquid silicon during the infiltration stage of the process. Thus, while all the carbides react with liquid silicon to form refractory silicides and new silicon carbide, this only significantly affected the reaction-bonding process if the dissolution/reaction kinetics were so fast as to disrupt the formation of the new silicon carbide framework which grows epitaxially to bond the existing silicon carbide particles together. As with conventional RBSC, the initial SiC grits play no part in any reaction except to act as nucleation sites for the new SiC. The microstructures of the various new materials have been characterized by reflected light microscopy, scanning electron microscopy, energy dispersive X-ray analysis and X-ray diffraction. This has led to an appraisal of the high-temperature reactions observed to have occurred and the unreliability of the high-temperature thermochemical data used to predict their occurrence. The mechanical properties of the new materials have been investigated by indentation testing (hardness and fracture toughness), including temperature-variant tests. Results are presented and the possibility for improving the properties of RBSC are discussed.

1. Introduction

The reaction-bonding process for silicon carbide essentially involves producing a fully dense ceramic body by infiltrating a porous compact of silicon carbide grit and finely divided carbon with liquid silicon ("siliconizing"). The carbon and silicon react *in situ* to produce new silicon carbide which bonds the compact together. By incorporating other materials into the initial compact, the process is potentially adaptable to the fabrication of more complex mixed-phase ceramics. The major aim of the study reported here has been to explore this possibility.

Reaction-bonded silicon carbide (RBSC) was first produced by Popper [1] in the early 1960s. The original material was inhomogeneous and had an uncontrolled microstructure. In the subsequent 30 years it has become possible to produce RBSC with a controlled, predictable microstructure which has good engineering properties, e.g. [2]. The microstructure of a typical recent RBSC material consists of about 90 vol % silicon carbide grains which are strongly bonded together into a continuous network, with the remaining volume occupied by silicon, as shown in Fig. 1. To produce such a final structure, the proportions of silicon carbide grit, finely divided carbon and porosity in the initial compact must be both carefully controlled and well mixed, e.g. [3]. This also prevents the occurrence of porosity and agglomerates in the resultant structure. The compact is then infiltrated with liquid silicon which reacts with the carbon in the compact to form "new" silicon carbide. This new SiC material usually nucleates heterogeneously on the existing SiC surfaces and grows to form an epitaxial overlayer on each original particle. Three-dimensional bonding of the silicon carbide network occurs by the impingement of these overgrowths on adjacent SiC particles.

The details of the microstructural evolution and evidence for epitaxial deposition of the new SiC have been given by Sawyer and Page [3] and Ness and Page [4]. An interesting point about the process is that, because of partition effects, most of the impurities in the silicon remain in solution and are eventually swept out on to the surface of the compact before solidifying as globules. A consequence of this behaviour is that the new SiC–SiC grain boundaries that are formed are generally clean and often relatively strong [4]. The resulting engineering ceramic is fully dense, has good resistance to chemical attack and reasonable fracture toughness and strength. RBSC has been widely utilized for its abrasion resistance in bearings and seals (e.g. in sewage pumps) and for its low unlubricated coefficient of friction in dry bearing systems [5].

0022–2461/92 $03.00 + .12

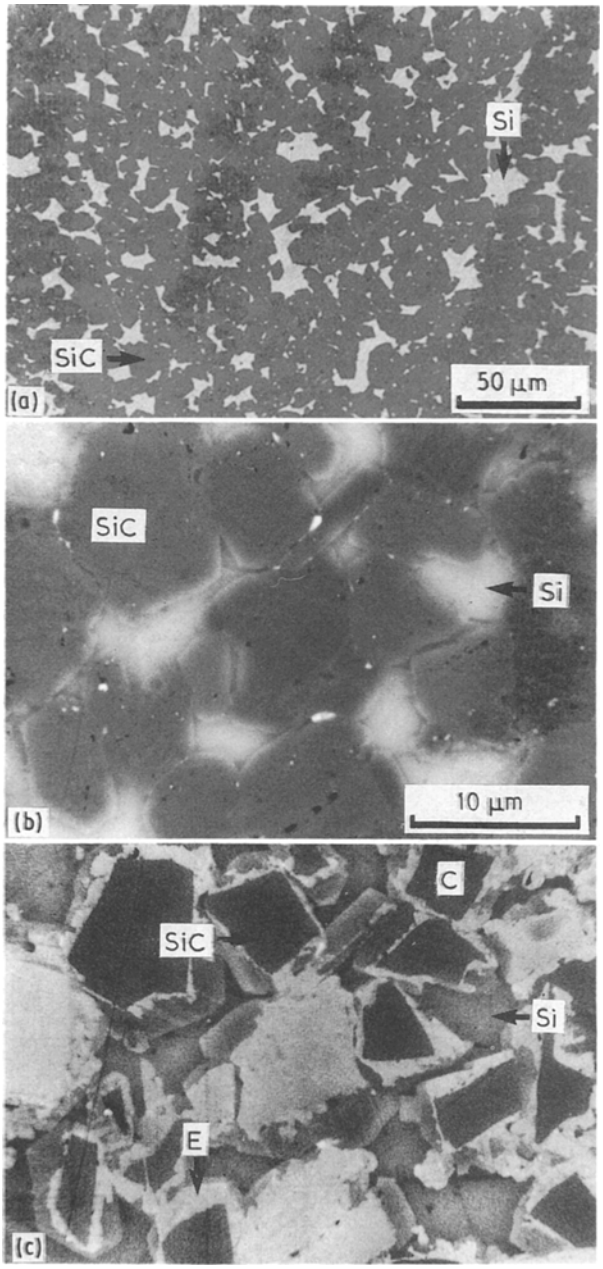

Figure 1 Micrographs showing microstructure of conventional reaction-bonded silicon carbide. (a) Light micrograph showing the two phases present. (b) SEM backscattered electron image showing atomic number contrast between silicon and silicon carbide. The small white particles are high atomic number silicides formed from impurities in the silicon used for infiltration. (c) SEM secondary electron image showing the bright-dark contrast within the silicon carbide grains characteristic of RBSC. The contrast in (c) is between the pre-existing SiC grit particles (C) and the epitaxial overlayers (E) of "new" SiC formed on them during reaction-bonding.

This paper reports some new developments to RBSC aimed at increasing its potential range of applications. The principal areas in which the performance of RBSC could be improved are its fracture toughness and the highest temperature at which it can be used without loss of structural integrity. In conventional RBSC, the upper temperature limit is usually governed by the melting of the remnants of the silicon infiltrant (the minority phase) at 1410 °C. However, the presence of some metallic impurities (e.g. alkaline earth metals) can result in the formation of low melting point silicides at the grain boundaries which can further reduce the upper temperature limit [4]. Initially our studies attempted to address the toughness problem by assessing the range of materials which might be developed together with their potential for "microstructural toughening", e.g. by crack deflection, microcrack formation, etc. [6]. Also some potential solutions to the service temperature problem have emerged, for example the replacement of the remnant silicon with a more refractory silicide.

The principal method chosen to alter the mechanical properties of RBSC was by the addition of a second phase to the initial mixture of SiC grit and carbon in replacement for a proportion of the silicon carbide. The materials to be added were chosen on the basis of their refractoriness, supposed chemical inertness, hardness and difference in elastic modulus compared with silicon carbide (for microcrack toughening). The prime candidates were refractory carbides, oxides and borides. The choice of the carbides, B_4C, TaC, TiC and ZrC, was based both upon their ready availability and their supposed thermodynamic stability with respect to silicon carbide at the reaction-bonding temperature, as shown in the free energy of reaction against temperature curves in Fig. 2 [7]: B_4C is less stable than SiC whilst the other three are more stable. TiB_2 was also used because of its reported efficacy in toughening hot-pressed silicon carbide by a microcracking mechanism [8]. The results of incorporation of a refractory oxide, ZrO_2, have been reported elsewhere [9].

A brief exploration of the mechanical properties was made by indentation testing. Properties measured

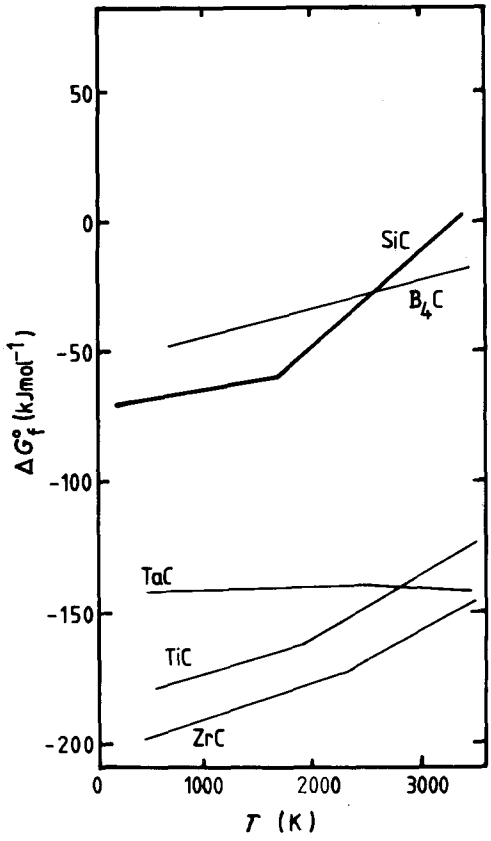

Figure 2 Gibbs' free energy of formation against temperature for a variety of carbides.

included the indentation hardness as a function of load and temperature and the indentation fracture behaviour.

2. Experimental procedure

2.1. Fabrication of materials

The mixed-phase RBSC materials were fabricated using the same SiC and carbon precursor materials and the same die-pressing compaction route as is used for conventional RBSC [2, 5] except that the batch size was much smaller. The initial powder mixtures were prepared such that the final microstructure would contain 15 vol % added phase, assuming that the added phase did not disrupt the reaction-bonding process. The dry powders were added together and mixed as a slurry in methylethylketone (MEK) using a "Z-blade" mixer. A proprietary polymeric binder was added to a carefully controlled level in order to provide green strength and control the level of porosity. Mixing continued for about 1 h. The MEK was allowed to evaporate and the remaining lumps were granulated by forcing through a sieve with a mesh size of approximately 1 mm. Any remaining MEK was driven off by heating to 60 °C overnight in an oven. The granules were shaped into cylindrical pellets of about 20 mm diameter and 10 mm high using a die-set in a hydraulic press. After green forming, the pellets were debonded (removal of binder) by slow heating to about 360 °C followed by a hold at temperature of 6 h. The binder was removed by a combination of evaporation and slow oxidation.

After debonding, the pellets were infiltrated with liquid silicon in a large cylindrical vacuum induction furnace. The pellets were placed on a carbon sheet resting on top of a carbon boat filled with silicon granules. The furnace temperature was raised to 1600 °C and held for 2 h to ensure that the reaction-bonding process was completed. After reaction bonding was complete, the pellets were allowed to cool slowly in the furnace.

2.2. Microstructural characterization methods

The microstructures of the reaction-bonded pellets were characterized in order to provide *post facto* evidence of the structural and chemical changes which had occurred during siliconizing. The techniques used included reflected light microscopy (RLM), scanning electron microscopy (SEM), energy dispersive X-ray analysis (EDX) and X-ray powder diffraction (XRD). RLM (Olympus BH-2) was used to examine the pellets for homogeneity and the presence of any unexpected reaction products. Initially SEM (CamScan S4-80DV) in secondary electron mode was used to look for contrast between the original SiC grits and their epitaxial overlayers of newly formed SiC. This unusual contrast has been critical in allowing the microstructural evolution of standard RBSC materials to be explored and relies on different concentrations of trace impurities altering the secondary electron emission of SiC, as in Fig. 1 [3, 4]. SEM was also used to determine the composition of individual grains by the use of *in situ* EDX analysis and back-scattered electron imaging. XRD (Hägg-Guinier camera with CuK_{α_1} radiation) was used for bulk phase determination.

Specimens for RLM, SEM and EDX were prepared by sectioning the pellets with a low-speed annular diamond saw, followed by lapping and polishing using successively finer diamond pastes down to a final size of 1 μm. Samples for XRD were prepared by crushing a small sample of each pellet in a tungsten carbide–cobalt percussion mortar and then grinding to a fine powder using an agate mortar and pestle.

2.3. Indentation testing methods

Indentation tests at room temperature were performed on the polished specimens used for LM and SEM using a microhardness tester. Loads ranging from 0.4905–9.81 N were used. Indentations were measured using an optical measuring head equipped with a vernier scale giving a potential accuracy in the measurements of ± 0.25 μm. However, the errors are greater than this because of uncertainty as to where the edge of the indentation should be taken together with the optical limitations (numerical aperture) of the microscope.

Hardness as a function of temperature was measured using a Wilberforce Scientific Developments high-temperature hardness testing machine [10]. Five to ten indentations were made at every 200 °C over the temperature range 200–1000 °C at a vacuum of better than 10^{-5} torr (1 torr = 1.333×10^2 Pa) using an indentation load of 4.905 N. The indentation diagonals were measured using the optical measuring head fitted to the Shimadzu microhardness tester.

Indentation fracture toughness was investigated using a standard Vickers hardness testing machine with loads in the range 9.81–98.1 N. Measurements of the median/radial crack lengths and indentation diagonals were again made using the Shimadzu measuring head.

3. Results and discussion

3.1. Microstructures and their evolution

Observations of the pellets upon removal from the furnace suggested that the normal reaction-bonding process had occurred in some cases but not in others: the RBSC–15 vol % ZrC pellet had a rough crust, the RBSC–15 vol % TiC pellet had a less significant crust and the RBSC–15 vol % TaC had grossly (and non-uniformly) expanded to no longer resemble the original pellet. However, the RBSC–15 vol % B_4C and RBSC–15 vol % TiB_2 pellets were very similar in appearance to an ordinary RBSC material.

3.1.1. RBSC–15 vol % TiB_2

Microstructural examination by RLM revealed that the RBSC–15 vol % TiB_2 had the simplest microstructure (Fig. 3a). In this case, the TiB_2 particles had substituted for some of the SiC grains with no sign of any reaction between the TiB_2 and any of the other phases present, especially the silicon. Fig. 3b is a

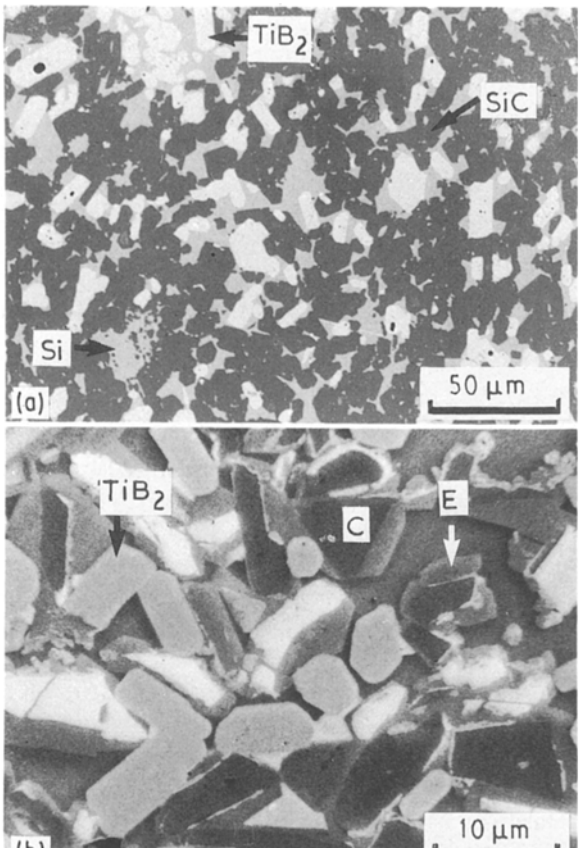

Figure 3 Micrographs of RBSC – 15 vol % TiB_2. (a) Light micrograph showing that there are three phases present, identified as SiC, Si and TiB_2. (b) SEM secondary electron image with the characteristic contrast between the grain cores (C) and the epitaxially deposited SiC (E) indicating that the reaction-bonding process has not been disrupted.

secondary electron SEM image and shows the contrast within the SiC grains establishing that the newly formed SiC has grown epitaxially on the original SiC grits. There is no obvious evidence either of any homogeneous nucleation of new SiC (sometimes present as fine, $\sim 1\,\mu m$, grains within the silicon in poorly mixed RBSC materials) or of any heterogeneous nucleation on the TiB_2 particles. In general, the TiB_2 grains are uniformly distributed with only small numbers of agglomerated particles.

Neither RLM nor SEM revealed any obvious cracks around the TiB_2 particles, and particle pull-out during polishing was not observed to occur, suggesting that the particles are well bonded into their matrix of silicon and silicon carbide. In order to produce a microstructure which provides toughening by generation of microcracks on application of a tensile stress, it would be necessary to adjust the TiB_2 particle size to just below the critical value for spontaneous generation of microcracks (e.g. [8]). In this case it appears that this critical size is greater than the added particle size of $\sim 10\,\mu m$. However, without details of the various interfacial toughnesses involved, further estimation of the critical size by calculation is difficult in mixed-phase systems of this kind.

3.1.2. RBSC–15 vol % ZrC

Light microscopy performed on sections through the RBSC–15 vol % ZrC pellet showed a crust about 1 mm thick around the outside which had a different microstructure compared with the centre of the pellet (Fig. 4). The centre of the pellet (Fig. 4a) consisted of three major phases identified by XRD analysis as silicon carbide, silicon and zirconium disilicide ($ZrSi_2$), with no lines present for zirconium carbide. In this case, silicon carbide was by far the majority phase, with the proportions of silicon and $ZrSi_2$ about equal. The micrographs show a significant level of voiding in some regions of the pellet; this is presumed to be due to grain pull-out during section preparation rather than incomplete reaction bonding, leaving residual carbon because, an excess of silicon was used specifically to avoid such problems. Further, because the silicon has obviously reacted with both the carbon and the ZrC, it seems unlikely that the porosity is an inherent feature of the microstructure due to incomplete wetting of the particulate array by the infiltrating silicon. Secondary electron scanning electron micrographs (Fig. 5a) show contrast in the SiC grains characteristic of epitaxial layer formation indicating that the reaction-bonding mechanism has not been disrupted by the added ZrC. Fig. 5b shows the distribution of the different phases revealed by atomic number contrast.

The outer crust of the RBSC–ZrC specimen (Fig. 4b) consists of the same three phases as the centre of the pellet, i.e. SiC, Si and $ZrSi_2$, although in this case silicon carbide is the minority phase and is far from uniformly distributed. Of the other two phases,

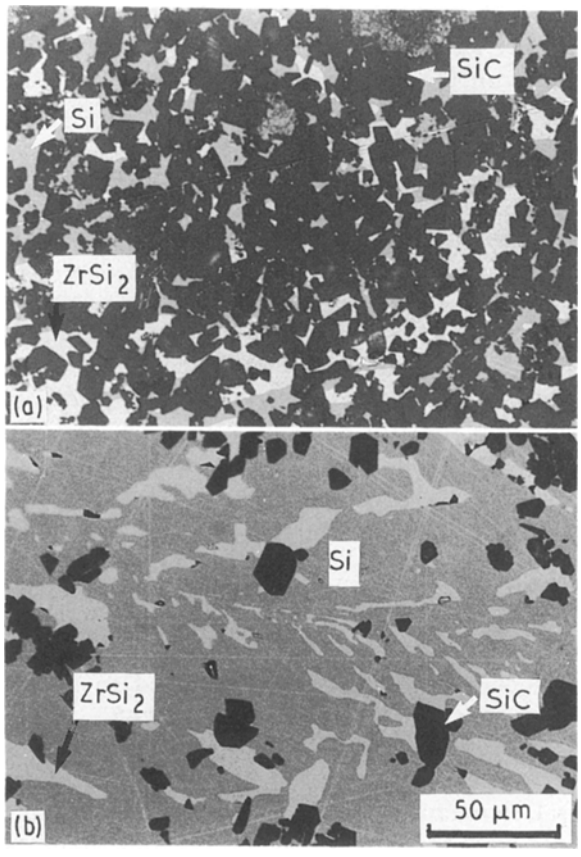

Figure 4 Light micrographs of the RBSC–15 vol % ZrC pellet. (a) The centre and (b) the outer crust showing the three phases present in each case.

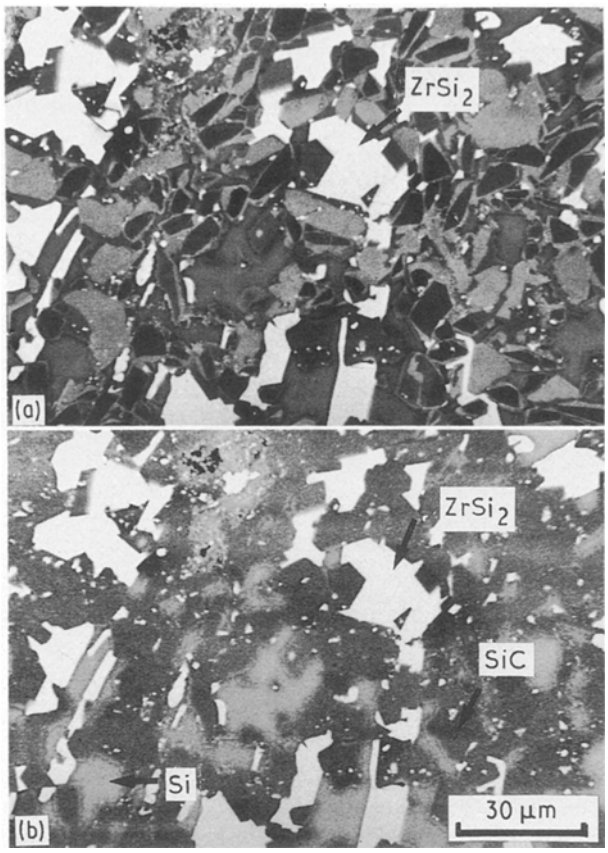

Figure 5 (a) SEM secondary electron image of the RBSC–15 vol % ZrC pellet showing that the reaction-bonding process has not been disrupted (cf. Fig. 1c). (b) SEM backscattered image showing the phase distribution by atomic number contrast.

quantitative EDX analysis suggests that the overall composition is very close to that of the eutectic in the silicon–zirconium system, i.e. 10 at % Zr–90 at % Si, which corresponds to volume fractions of 73% Si and 27% $ZrSi_2$. A manual area fraction analysis using scanning electron micrographs yields a very similar result. The fact that the outer crust is of the eutectic composition suggests that during cooling the lower melting point material in the crust was the last to solidify and was probably squeezed out by proeutectic silicon or zirconium silicide solidifying and expanding within the pellet. The small number of silicon carbide grains present were probably swept away from the outer surface of the pellet as the eutectic liquid was forced out.

When the microstructure of the RBSC–ZrC pellet is considered in conjunction with the silicon–zirconium phase diagram, Fig. 6 ([11], p. 1205), it appears likely that the zirconium content of the silicon did not exceed about 22 at % in the bulk of the sample (i.e. to the left-hand side of the ZrSi liquidus line) because no ZrSi was found. Such high zirconium concentrations could only be produced if the dissolution rate of the ZrC particles was high enough and the rate of zirconium transport away from the dissolution site low enough. The fact that such high zirconium concentrations apparently did not occur suggests either that the ZrC dissolution rate is slow or the zirconium transport fast. Further, the fact that no remnants of ZrC particles were found surrounded by a

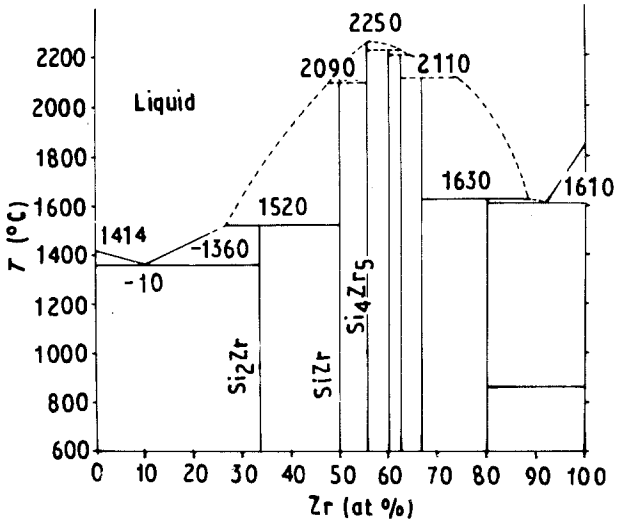

Figure 6 Silicon–zirconium binary equilibrium phase diagram ([11], p. 1205).

shell of silicide suggests that the dissolved zirconium was transported rapidly away from the dissolution site.

3.1.3. RBSC–15 vol % TiC

The microstructure of the bulk of the sample is similar to that of the RBSC–ZrC pellet, although the network of silicon carbide is less continuous. This is shown in Fig. 7. The centre of the pellet largely consists of three phases, SiC, silicon and titanium disilicide ($TiSi_2$), identified by a combination of XRD, EDX analysis and back-scattered electron imaging in the SEM. Traces of what are believed to be the initial titanium carbide particles were found: some individual particles gave strong TiK_α X-ray peaks, but a very weak SiK_α peak in comparison with $TiSi_2$. The intensity of the CK_α peak is so affected by absorption by higher atomic number elements that it can only be used to comment on the presence or absence of carbon in a particular location. Small amounts of a titanium silicide richer in titanium than $TiSi_2$ were found around

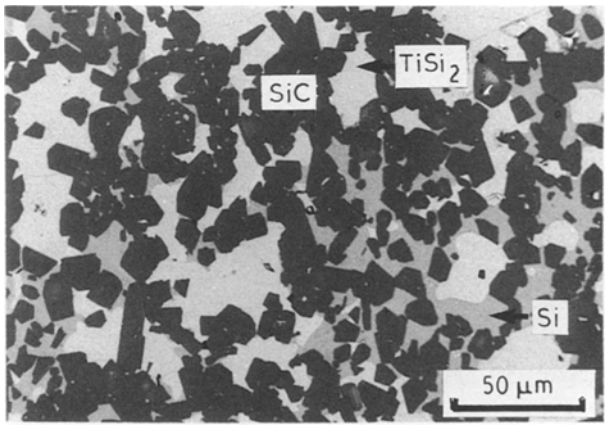

Figure 7 Light micrograph of a polished section from the RBSC–15 vol % TiC pellet showing the microstructure of the centre. Three phases are present, silicon carbide being the majority phase, with the proportions of the other two approximately equal.

the TiC remnants. The contrast between the epitaxial overlayers and the cores of the SiC particles in SEM secondary electron images (Fig. 8) again indicates that the reaction-bonding process has not been disrupted.

The outer crust of the RBSC–15 vol % TiC pellet is different from that of the RBSC–ZrC pellet in that it is much thinner, but more complex in microstructure. Back-scattered SEM imaging (Fig. 9) combined with EDX analysis indicates the presence of five phases; these are silicon, silicon carbide, titanium disilicide, titanium carbide remnants and a titanium–silicon compound of higher atomic number per unit volume than $TiSi_2$ (e.g. TiSi or Ti_5Si_3). The $TiSi_2$ and silicon are present at the extreme outside as a localized globular eutectic, with the other phases between this and the bulk of the pellet. The presence of a titanium-rich silicide suggests that the liquid which formed the crust was considerably hypereutectic.

The microstructural evolution of this material appears broadly similar to that of RBSC–ZrC material as might be inferred from their similar phase diagrams (Figs 6 and 10), the differences arising from the different levels of supersaturation reached by the infiltrating silicon.

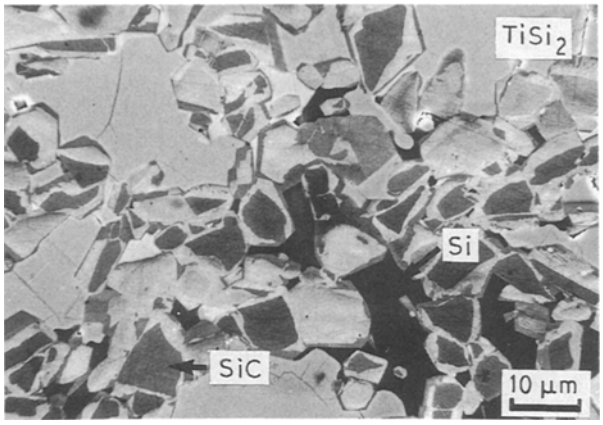

Figure 8 SEM secondary electron micrograph of the centre of the RBSC–15 vol % TiC pellet showing the presence of epitaxial coatings on the SiC grains together with two other phases, silicon and $TiSi_2$.

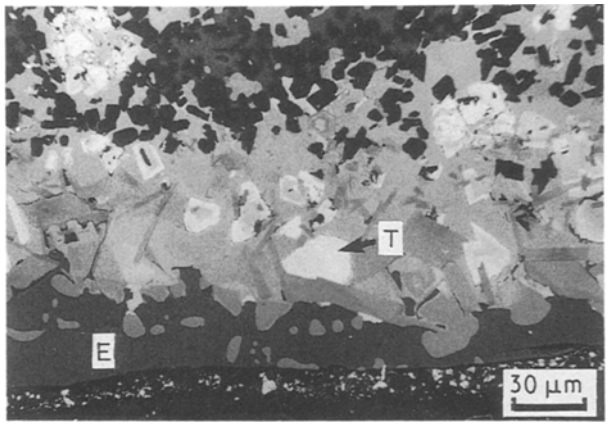

Figure 9 Backscattered SEM image of the outer crust of the RBSC–15 vol % TiC pellet showing its complex structure and the variety of phases present. At the extreme outside edge is an Si–$TiSi_2$ eutectic structure (E), whilst further from the edge are large Ti–Si particles (T), richer in titanium than would be the case for $TiSi_2$.

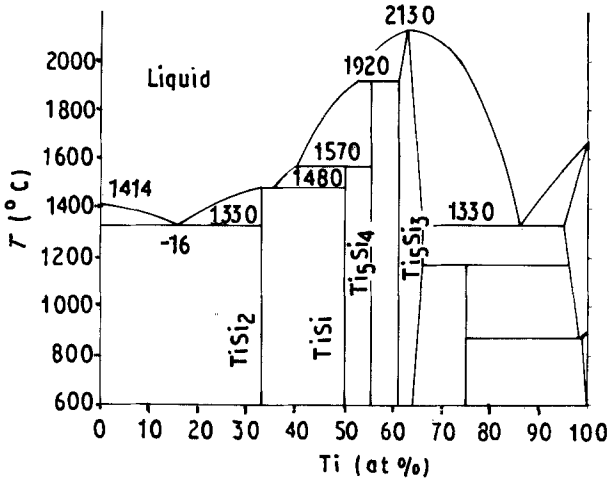

Figure 10 Silicon–titanium binary equilibrium phase diagram ([11], p. 1197).

3.1.4. RBSC–15 vol % TaC

The ex-furnace appearance of the RBSC–15 vol % TaC pellet was very different from that of the other pellets: the pellet had completely lost its integrity and resembled a lump of slag. Polished sections (Fig. 11) revealed that majority of the pellet was silicon with a non-uniform distribution of silicon carbide grains (clusters up to 500 μm in size separated by channels of silicon) and occasional large angular particles identified by quantitative EDX as $TaSi_2$. The probable cause of the uncontrolled expansion of the RBSC–TaC pellet is best considered in conjunction with the silicon–tantalum equilibrium phase diagram, Fig. 12 ([11], p. 1194). In comparison with both the Si–Zr and Si–Ti phase diagrams, the liquidus line between $TaSi_2$ and the Ta–Si eutectic is very much steeper and the eutectic composition is at a much lower atomic fraction. As a result, the tantalum concentration at the reaction-bonding temperature at which the liquid silicon becomes saturated is lower than in the other two systems. Thus $TaSi_2$ precipitation begins much earlier and the possibility exists of

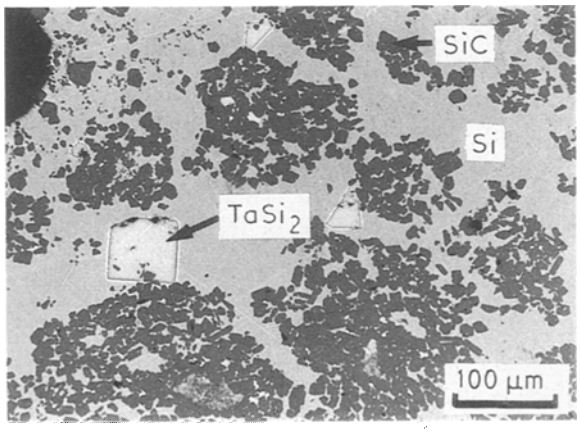

Figure 11 Light micrograph of the RBSC–15 vol % TaC pellet showing clusters of silicon carbide grains, wide channels of silicon and large angular particles of $TaSi_2$.

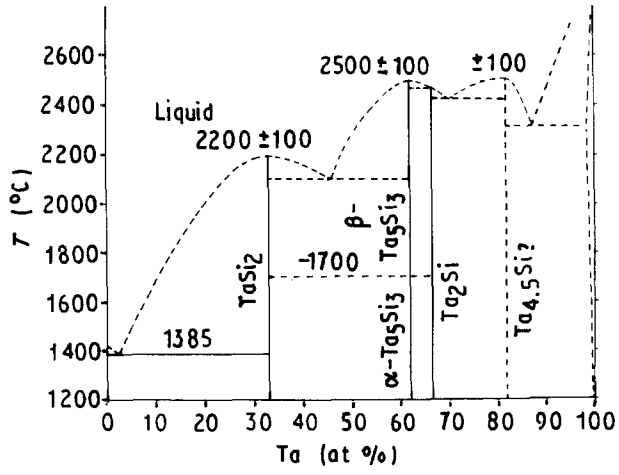

Figure 12 Silicon–tantalum binary equilibrium phase diagram ([11], p. 1194).

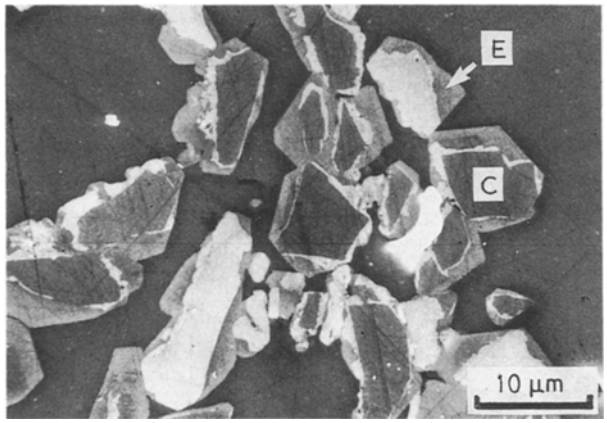

Figure 13 Scanning electron micrograph of the RBSC–15 vol % TaC pellet showing the secondary electron contrast between the epitaxial layers (E) and grain cores (C) indicating that the reaction-bonding chemistry has not been disrupted.

large primary $TaSi_2$ crystallites pushing the SiC grains apart before they have become firmly bonded together. This would result in the open structure shown in the micrographs. The apparent absence of any obvious Si–$TaSi_2$ eutectic is probably explained by the volume fractions of the two phases in the eutectic being 0.935 Si and 0.065 $TaSi_2$. With this distribution of phases it is unlikely that a lamellar structure will be observed, though liquid of eutectic composition was almost certainly present.

Secondary electron imaging in the SEM (Fig. 13) reveals the new SiC epitaxial layers on the original SiC grits and thus establishes that the expansion of the pellet has not disrupted the reaction-bonding mechanism, although it has clearly resulted in the partial dispersion of the SiC grains before the epitaxial layers had impinged and bonded the SiC framework together. Also, no homogeneously nucleated silicon carbide, is evident. The occurrence of homogeneously nucleated new SiC usually results from an absence of local heterogeneous nucleation sites in inhomogeneous compacts. In this case their absence is quite surprising because the maximum carbon diffusion distances (the separation between the SiC grains) are larger than would be the case in an ordinary RBSC compact.

3.1.5. RBSC–15 vol % B_4C

The RBSC–15 vol % B_4C pellet had a fairly smooth surface on removal from the reaction-bonding furnace. Measurements suggested that the pre-bonding shape of the pellet had been retained. Reflected light micrographs of polished sections through the pellet indicated the presence of two distinct regions: in the centre, the B_4C particles were intact, although often cracked (Fig. 14a); whilst at the outside there were large pockets of silicon containing a dispersion of very large silicon carbide grains (Fig. 14b). These silicon pockets are slightly smaller than the original B_4C particles (roughly 100 μm diameter).

The initial stability criterion used for selecting the added third phase suggested that B_4C was less stable than SiC at the reaction-bonding temperature. Something might, therefore, have been expected to happen during the high-temperature processing stage. EDX elemental mapping suggests that attack of the added phase by the infiltrating silicon has again occurred, whilst secondary electron SEM imaging shows that the outer edges of the B_4C grains have "fingers" of a second phase running into them (Fig. 15). The composition of this phase has not yet been determined, but

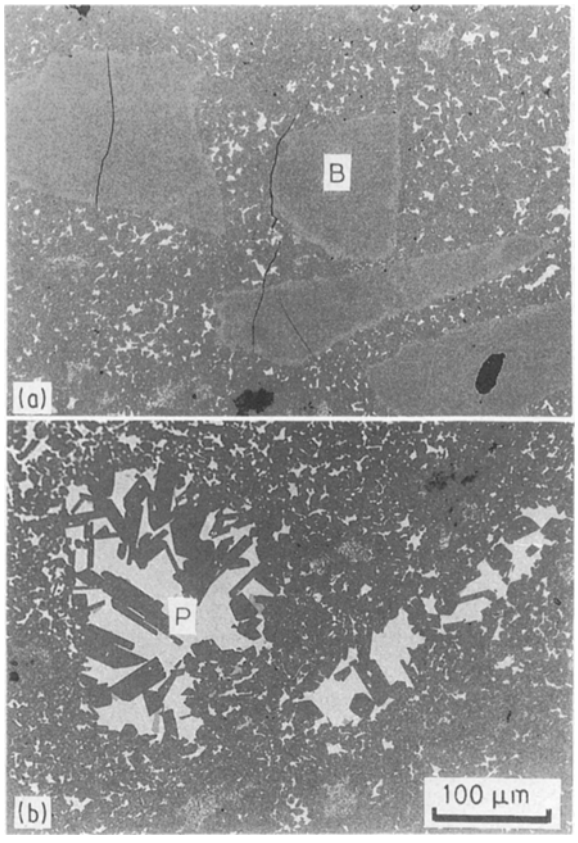

Figure 14 Light micrographs of the RBSC–15 vol % B_4C pellet. (a) The centre of the pellet showing the presence of large B_4C grains (B) which show signs of chemical attack at their outer edges. (b) Near the surface of the pellet, showing the absence of large B_4C grains, but the presence of pockets (P) of roughly the same size containing large SiC grains.

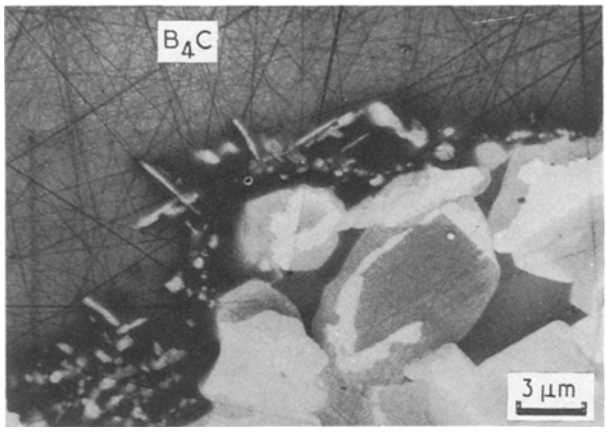

Figure 15 SEM secondary electron image of a B_4C particle in the centre of the RBSC–15 vol % B_4C pellet. The edge of the particle is being attacked with "fingers" penetrating from the surface.

two possibilities are that it is a boron–silicon binary compound or a boron–silicon–carbon ternary compound.

The morphology of the large silicon carbide grains at the outside of the pellet are very similar to the large tabular recrystallized SiC grains seen in hot-pressed silicon carbide which has had boron carbide added to promote densification [12]. The similarity in size between the regions of (exaggerated) grain growth and the original B_4C grains suggests that one has replaced the other. The carbon from the B_4C is probably incorporated into the large SiC grains by reaction with liquid silicon. The volume of silicon carbide present within the pockets would be about 10% of the volume of the original B_4C grain if the only carbon source was the B_4C grain; in this case the SiC content is somewhat greater, suggesting some carbon transport into the pocket from its surroundings. Neither secondary electron imaging (Fig. 16) nor etching (using an oxidizing chromic acid electrolytic etch [13]) revealed any epitaxial overlayer on any of these grains which suggests that they were formed by homogeneous nucleation within pockets of liquid silicon. For those pockets close to the outside of the pellet, it was not possible to detect any boron using a windowless EDX detector and it is assumed that (apart from incorporation of a small amount into the growing SiC grains) most of the boron has been lost to the furnace atmosphere, possibly as B_2O_3.

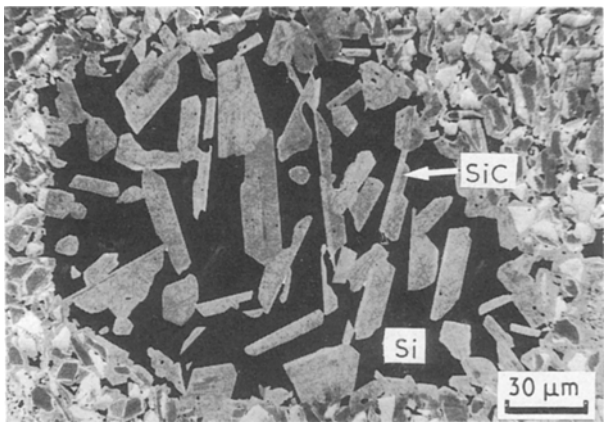

Figure 16 SEM secondary electron image of the large SiC grains in a pocket near the edge of the RBSC–15 vol % B_4C pellet. These large grains do not show the normal core + epitaxial layer secondary electron contrast (of the smaller surrounding SiC grains).

The homogeneous nucleation of silicon carbide within the pockets left by the B_4C particles is probably promoted by the large distances which carbon would be required to diffuse if it were to be epitaxially deposited on the pre-existing SiC grains around the pocket. Thus the size of these pockets provides an upper limit of $\sim 40\,\mu m$ on the carbon diffusion distance during the reaction-bonding process. The number of nuclei formed is probably limited by the relatively slow release of carbon from the B_4C grains compared with the dissolution rate for a large number of sub-micrometre graphite particles. As a result a small number of large grains is observed rather than a large number of very fine grains.

3.2. The reaction-bonding process in mixed-phase materials

In all the above cases, the addition of the third phase has not disrupted the reaction-bonding chemistry whereby the infiltrating silicon reacts with the carbon to form new SiC. The deposition mechanism for this new SiC is also unaffected because, in every case, epitaxial layers are formed showing that the nucleation of the newly formed SiC is dominated by heterogeneous nucleation on the existing SiC. No obvious nucleation of SiC on the other solid phases either present in the original compact or formed during silicon infiltration was seen. This may simply reflect a structural preference for SiC as a nucleation site.

For the RBSC–ZrC and RBSC–TiC cases it is interesting to note that the eventual squeezing out of liquid to the exterior of the compact implies that the framework of reaction-bonded SiC crystals existed before completion of the metal carbide–silicon reactions. This suggests a two-stage process occurring: the Si–C reaction occurring first and being quickly completed, the other reaction being slower. This sequence is important in preserving the size and shape of the pellet during reaction bonding and thus allowing near-net-shape forming. Besides any intrinsic kinetics, there are two factors governing this sequence. Firstly, the metal silicides produced from the added carbides cannot form until at least some of the carbide has dissolved. Secondly, the concentration of carbon which saturates liquid silicon at 1600 °C ($\sim 5 \times 10^{-2}$ at % [14]) is very much smaller than the concentration of the relevant metal (> 10 at %).

In the case of the RBSC–TaC material, the microstructural evidence suggests that although the reaction-bonding process successfully deposited new SiC on the original grits, structural bonding by the impingement of the various epitaxial overgrowths was not complete at the point at which $TaSi_2$ precipitation began and expanded the pellet. Thus near-net-shape forming was not possible.

The materials described above all demonstrated one of the primary requirements for producing a reaction-bonded material: the infiltrating silicon wetted all the

components of the compact. With RBSC–TiB_2, wetting was not accompanied by any obvious signs of reaction (although this may have occurred in a very narrow band adjacent to the interface), whilst for the other four compositions, reaction was very significant or complete. These observations still do not allow the question of whether or not some degree of reaction is necessary to promote wetting, to be answered. However, if the degree of wetting within the compact is reduced such as by the addition of alumina, a phase not wetted by silicon, the rate of infiltration is dramatically reduced [15].

However, it is interesting to note that liquid silicon will behave as a metallic conductor as far as adhesion and wetting is concerned in that it will be able to support the induced charges necessary according to the models of Stoneham and Tasker [16]. Silicon may thus be an unusual infiltrant because it has good, metal-like wetting properties with liquid and ceramic-like properties after solidification.

3.3. Thermodynamics and the fabrication of mixed-phase reaction-bonded materials

It should have been possible to predict that the reactions which took place in the pellets would have occurred by the use of high-temperature thermochemical data compilations. As a *post facto* exercise to see if this would indeed have been possible, a range of data on the various components in the systems was gathered. There are some fairly extensive tabulations of thermo-chemical data in, for example, Kubaschewski and Alcock [17] and the Joint Army, Navy, Air Force (JANAF) Thermochemical Tables [18]. There are drawbacks with the data, the most serious of which is that it is not comprehensive; a particular problem in this case is that there are very few data on transition metal silicides formation. Another serious problem is that in many cases thermochemical data are only quoted for 298 K, necessitating calculation to obtain values for elevated temperatures.

TABLE I Standard enthalpies and entropies at 298 K for a variety of elements and compounds used in the fabrication of silicon carbide-based mixed-phase materials

Element or compound	ΔH^0_{298} (kJ mol^{-1})	ΔS^0_{298} (J mol^{-1} K^{-1})	Reference
$Si_{(s)}$	–	18.83 ± 0.21	[17]
$Si_{(l)}$	+ 455.7 ± 5.0	167.90	[17]
$SiC_{(s)}$	− 67.0 ± 6.3	16.53 ± 0.21	[17]
$TaC_{(s)}$	− 143.1 ± 3.3	42.39 ± 0.84	[17]
$TaSi_{2(s)}$	− 119.3 ± 12.6	75.3 ± 6.7	[17]
$Ta_2Si_{(s)}$	− 125.6 ± 25.1	105.5 ± 11.7	[17]
$Ta_5Si_{3(s)}$	− 334.8 ± 33.5	280.8 ± 27.2	[17]
$TiC_{(s)}$	− 183.7 ± 6.3	24.3 ± 0.8	[17]
$TiSi_{2(s)}$	− 134.3 ± 20.9	61.1 ± 9.2	[17]
$TiSi_{(s)}$	− 129.7 ± 14.6	49.0 ± 7.5	[17]
$ZrC_{(s)}$	− 202.01 ± 2.51	33.2 ± 2.1	[17]
$ZrSi_{2(s)}$	− 149.4	n/a	[19]
$ZrSi_{(s)}$	− 148.1	n/a	[19]
$TiB_{2(s)}$	− 323.9 ± 3.8	28.5 ± 0.46	[17]
$B_4C_{(s)}$	− 71.6 ± 11.7	27.12 ± 0.17	[17]

The most important thermochemical parameter in determining whether a reaction will proceed or not is the Gibbs' free energy of the reaction, ΔG^0; if this is negative then the reaction is thermodynamically favoured (although not necessarily kinetically favoured). Gibbs' free energies of formation are often presented as equations

$$\Delta G^0_T = A + BT\log T + CT \quad (1)$$

where A, B and C are constants and T is the absolute temperature, which allow the value of ΔG^0 to be calculated at any temperature. Such equations are produced from Gibbs' free energies of formation of the individual reactants and products, which are themselves often obtained from experimentally determined temperature variation of specific heat capacities. In the absence of such a free energy equation, the value of ΔG must be calculated using

$$\Delta G^0_T = \Delta H^0_{298} + \int_{298}^{T} \Delta C_p dT - T\Delta S^0_{298} - T\int_{298}^{T} \frac{\Delta C_p}{T} dT \quad (2)$$

where ΔH^0_{298} is the enthalpy change at 298 K, ΔS^0_{298} is the entropy change at 298 K and ΔC_p is the difference in molar specific heat capacities between the products and reactants.

For reactions of the type which are known to have occurred in three of the materials reported here, the generalized equation for the reaction is

$$MC + 3Si \rightarrow MSi_2 + SiC \quad (3)$$

Expressions giving the temperature variation of Gibbs' free energy of formation are readily available for all the species concerned apart from some of the silicides. All the data are given in Tables I and II. The

TABLE II Gibbs' free energies of formation as a function of temperature for a variety of carbides, borides and silicides

Compound	ΔG^0 (J mol^{-1})	Error (kJ mol^{-1})	Temperature range (K)	Reference
$Si_{(s)} + C_{(s)} = SiC_{(s)}$	− 51 900 + 2.09T	n/a	298–1686	[20]
$Si_{(s)} + C_{(s)} = SiC_{(s)}$	− 58 600 − 5.4T log T + 23.77T	± 10.5	298–1686	[17]
$Si_{(l)} + C_{(s)} = SiC_{(s)}$	− 113 400 − 11.43T log T + 75.7T	± 8.4	1686–2000	[17]
$Ta_{(s)} + 2Si_{(s)} = TaSi_{2(s)}$	− 129 300 + 4.051T	n/a	298–1686	[21]
$Ta_{(s)} + C_{(s)} = TaC_{(s)}$	− 146 000 + 2.09T	n/a	1250–1400	[17]
$Zr_{(s)} + C_{(s)} = ZrC_{(s)}$	− 184 600 + 9.2T	± 12.6	298–2200	[17]
$Ti_{(s)} + C_{(s)} = TiC_{(s)}$	− 183 100 + 10.09T	± 12.6	298–1155	[17]
$Ti_{(s)} + C_{(s)} = TiC_{(s)}$	− 186 600 + 13.22T	± 12.6	1155–2000	[17]
$4B_{(s)} + C_{(s)} = B_4C_{(s)}$	Data not available			
$Ti_{(s)} + 2B_{(s)} = TiB_{2(s)}$	Data not available			

TABLE III Calculated Gibbs' free energies of reaction for the formation of silicides from carbides at 1883 K

Reaction	ΔG^0_{1883} (kJ)	Error (kJ)
$TaC + 3Si \rightarrow TaSi_2 + SiC$	− 19.2	± 20.0
$ZrC + 3Si \rightarrow ZrSi_2 + SiC$	Insufficient data available	
$TiC + 3Si \rightarrow TiSi_2 + SiC$	− 0.8	± 20.0
$TiC + 2Si \rightarrow TiSi + SiC$	− 5.4	± 20.0
$B_4C + (4n + 1)Si \rightarrow 4BSi_n + SiC$	Insufficient data available	

results of the free energy of reaction calculations are shown in Table III. It can be seen that for those reactions for which enough data were available to perform a calculation, the values of ΔG^0 are very close to zero with errors (estimated from the errors in the original data) that are greater than the values themselves. This suggests that even with sufficient prescience to perform thermochemical calculations on potential reactions, the likelihood of making a correct prediction is low. With such a large error range, the possible outcomes range from no reaction to complete reaction in terms of calculated equilibrium constants. As a consequence the only way of testing whether a particular mixture of phases will remain stable is to try and make it.

In the case of the RBSC–15 vol % TiB_2 pellet no reaction was observed. When the highly exothermic Gibbs' free energy of formation of TiB_2 compared with the metal carbides is noted this is not surprising. For the reaction

$$TiB_2 + (2n + 2)Si \rightarrow TiSi_2 + 2BSi_n \quad (4)$$

to proceed would require the BSi_n compound formed to have a large negative free energy of formation. However, it is not possible to calculate the free energy change because data on boron silicides are not readily available.

3.4. Indentation testing

The results of the indentation testing are given in three parts: firstly the variation of hardness with load; secondly the variation of hardness with temperature at fixed load; and thirdly the indentation fracture behaviour.

3.4.1. Variation of hardness with load

The results of the microhardness testing are given in Table IV as the Vickers microhardness at 0.4905 N, 4.905 N, an indentation size effect (ISE) index and a calculated hardness for an indentation of 10 μm diagonal. For comparison, results from a conventional RBSC material ("REFEL") are also given. All the materials show a higher microhardness at low loads than at high loads. The materials in which the hard carbide phase has been replaced by a silicide are softer than conventional RBSC, particularly at high loads, whilst the materials in which reaction has been less extensive or nonexistent have microhardness values comparable with RBSC. The microhardness against load curves for the six materials are shown in Fig. 17. The curves are fitted to the load–diagonal data by the method of least squares after a ln–ln transformation [22]. The fitted curve is thus of the form

$$L = ad^n \quad (5)$$

where L is the applied load, a is a constant determined from the curve fitting (and is essentially a hardness value at a particular indentation size, e.g. 10 μm diagonal), d is the indentation diagonal and n is the ISE index. It must be emphasized that this expression is empirical but gives a measure, through the ISE index, of the deviation of the material from constant hardness at all loads ($n = 2$). However, previous work has shown that the constants a and n are often characteristic of a given material in a particular microstructural state. These parameters also provide a means of comparing the indentation hardness of two materials at the same indentation size rather than at the same indentation load [22]. The lower the value of the ISE index the greater the drop in the materials hardness as the indentation load is increased. One factor controlling ISE behaviour is the scale of the microstructure relative to the size of the indentation-affected volume; ISE effects also occur in single crystals, and recently there have been attempts to explain ISE behaviour in terms of scale effects in fundamental deformation mechanisms [23]. One important consequence of ISE behaviour is that the materials hardness at the small scales relevant to wear are not the same as values as those measured at larger scales using conventional hardness tests.

All the materials show similar values of n, which might be expected because their hardnesses are probably dominated by their connected silicon carbide framework (this being the dominant phase present). However, there is a trend for the hardness at a given indentation size to decrease with increasing silicon

TABLE IV Room-temperature hardness parameters for the RBSC materials reported in this study. "REFEL" RBSC is a commercial material supplied by UKAEA. The error values for $H_{0.4905\,N}$ and $H_{4.905\,N}$ are given as $\pm 2\sigma/n^{1/2}$. The $H_{10\,\mu m}$ value is calculated from the ISE index and provides a means of comparing the materials at the same scale of deformation

Material	$H_{0.4905\,N}$ (GPa, $\pm 2\sigma/n^{1/2}$)	$H_{4.905\,N}$ (GPa, $\pm 2\sigma/n^{1/2}$)	$H_{10\,\mu m}$ (GPa)	ISE index ($\pm 2\sigma$)
"REFEL" RBSC	27.5 ± 1.9	21.1 ± 1.5	25.76	1.772 ± 0.040
RBSC – 15 vol % ZrC	26.5 ± 3.0	20.4 ± 1.7	23.29	1.775 ± 0.054
RBSC – 15 vol % TiC	18.9 ± 4.6	15.1 ± 2.0	16.35	1.881 ± 0.102
RBSC – 15 vol % TaC	15.2 ± 3.4	13.2 ± 1.5	14.95	1.884 ± 0.073
RBSC – 15 vol % B_4C	30.4 ± 1.7	24.5 ± 1.7	28.02	1.827 ± 0.046
RBSC – 15 vol % TiB_2	28.5 ± 2.9	17.7 ± 2.3	23.25	1.686 ± 0.053

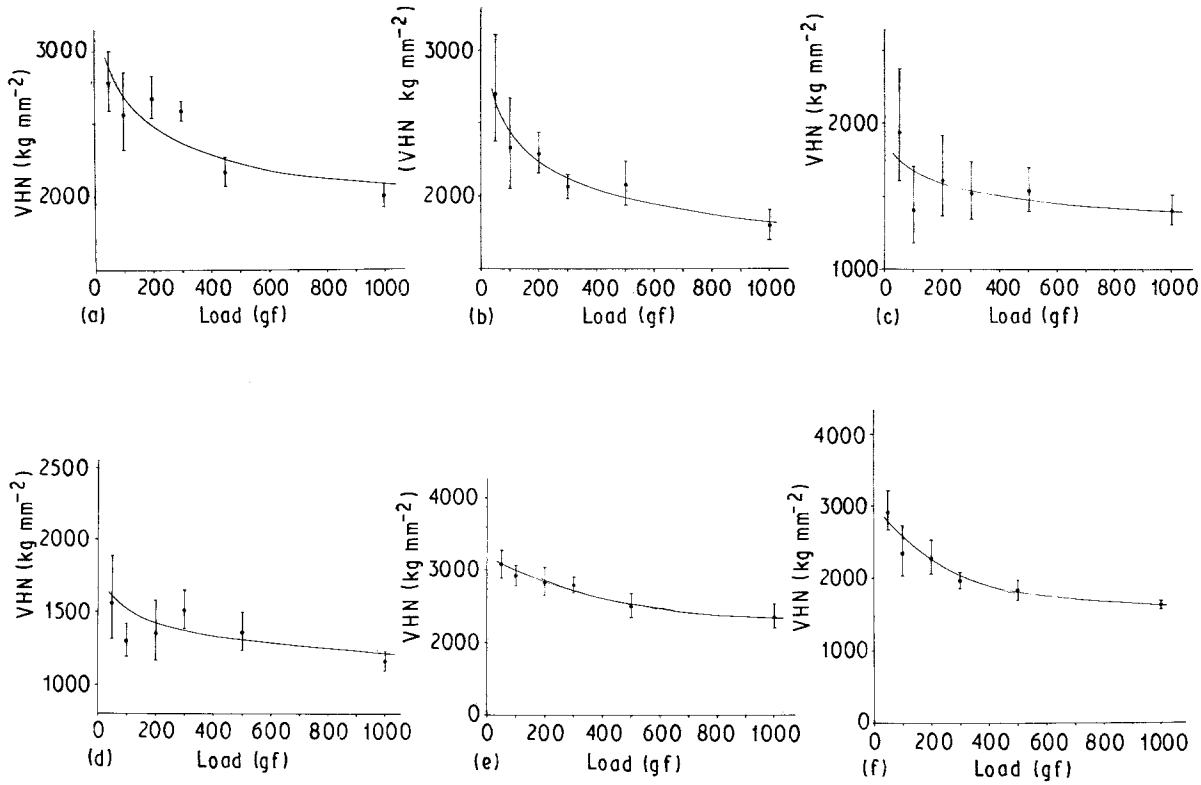

Figure 17 Graphs showing the Vickers microhardness as a function of load for (a) conventional RBSC, (b) RBSC – 15 vol % ZrC, (c) RBSC – 15 vol % TiC, (d) RBSC – 15 vol % TaC, (e) RBSC – 15 vol % B_4C, and (f) RBSC – 15 vol % TiB_2. The error bars represent $\pm 2\sigma/n^{1/2}$.

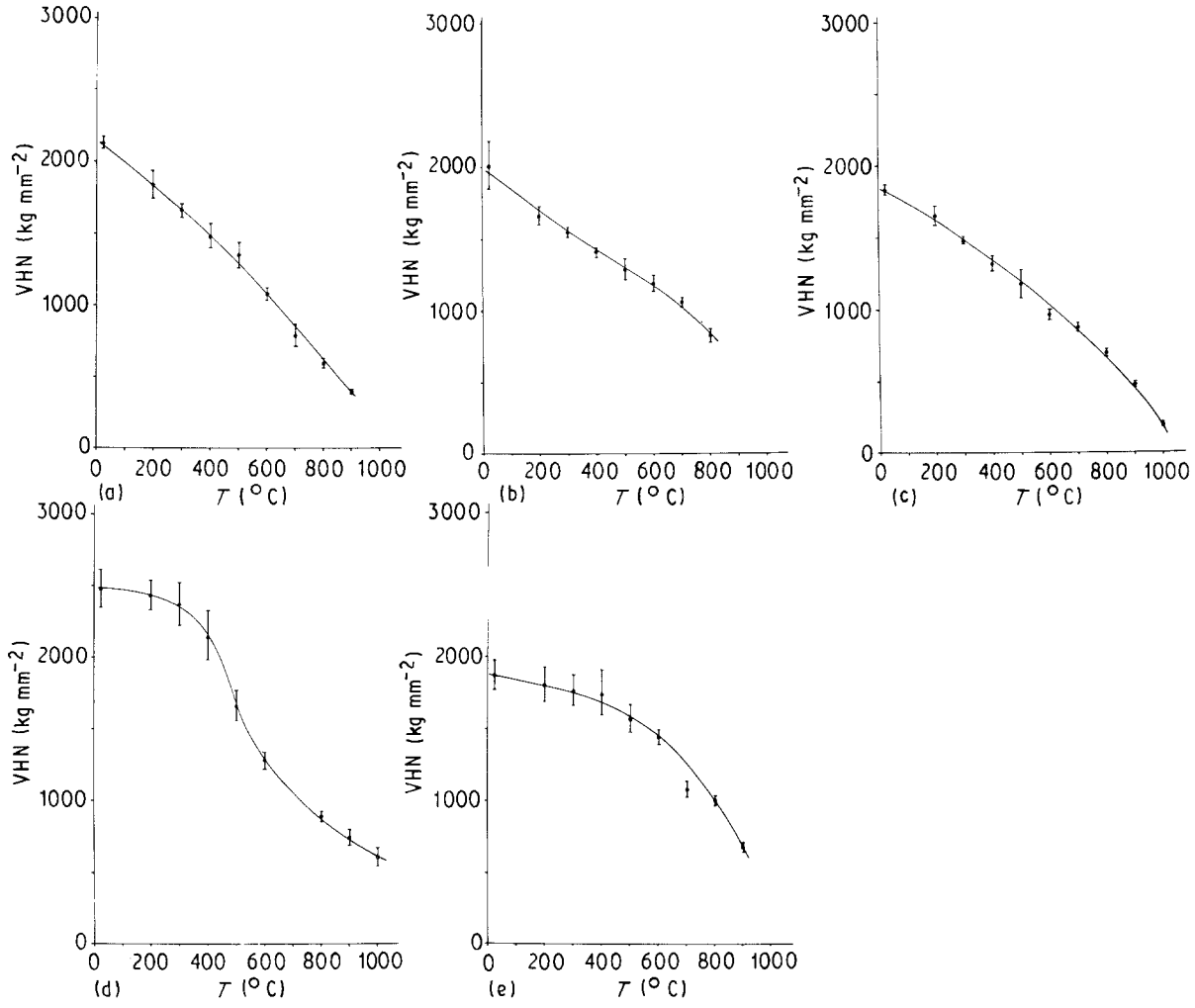

Figure 18 Graphs showing the variations of Vickers microhardness as a function of temperature at an indentation load of 4.905 N, for (a) conventional RBSC, (b) RBSC – 15 vol % ZrC, (c) RBSC – 15 vol % TiC, (d) RBSC – 15 vol % B_4C and (e) RBSC – 15 vol % TiB_2. The error bars represent $\pm 2\sigma/n^{1/2}$.

content. While most materials show values less than standard RBSC, the RBSC–B_4C material appears harder. This is expected because B_4C is harder than both silicon and silicon carbide. The RBSC–B_4C material also shows a high hardness at the small indentation sizes relevant to wear, as does the RBSC–TiB_2 material (Fig. 17). Microhardness tests indicate that in the case of the RBSC–ZrC material, the silicide in the eutectic outer layer has very nearly the same hardness as polycrystalline silicon: at an indentation load of 0.981 N, silicon has a measured Vickers hardness of approximately 10.1 GPa, whilst the $ZrSi_2$ was found to have a hardness of 10.3 GPa. The value for $ZrSi_2$ is close to the value of 10.1 GPa previously quoted by Schwarzkopf and Kieffer [24].

One problem recognized with this type of study is that progressively smaller indentations sample progressively smaller microstructural volumes. The chance of sampling a single grain with an indentation is increased and is one source of the increased variation in microhardness at small indentation sizes.

3.4.2. Variation of hardness with temperature

Temperature-variant microhardness testing provides a convenient means of exploring the temperature dependence of the mechanical properties of materials using small samples. Hence the Vickers microhardness of all the materials except RBSC–15 vol % TaC was measured as a function of temperature at a constant indentation load of 4.905 N. The raw hardness against temperature curves are shown in Fig. 18. They indicate that the hardness falls from its room-temperature value as the temperature rises. Replotting the data as $\ln(H)$ against $1/T_{(absolute)}$ (Fig. 19) reveals the temperature sensitivity of the deformation process(es). The two line segments on each graph were fitted by the method of least squares. The activation energies of the processes taking place can be obtained from the gradients of the line segments. This was first reported for indentation testing by Atkins *et al.* [25]. The expression [10]

$$\frac{H_1}{H_2} = \exp\frac{Q}{mRT}\left(\frac{1}{T_1} - \frac{1}{T_2}\right) \quad (6)$$

was used to calculate the activation energies in which H is the hardness, T the absolute temperature, Q the activation energy, R the molar gas constant and m a constant which depends on the strain rate and which we have taken to be 9 (as have other authors [10, 26]), even though it is known to vary with temperature. The activation energies calculated from this expression for the two line segments of each graph are given in Table V together with the transition temperature (T_{Trans}) from the low-temperature (LT) to high-

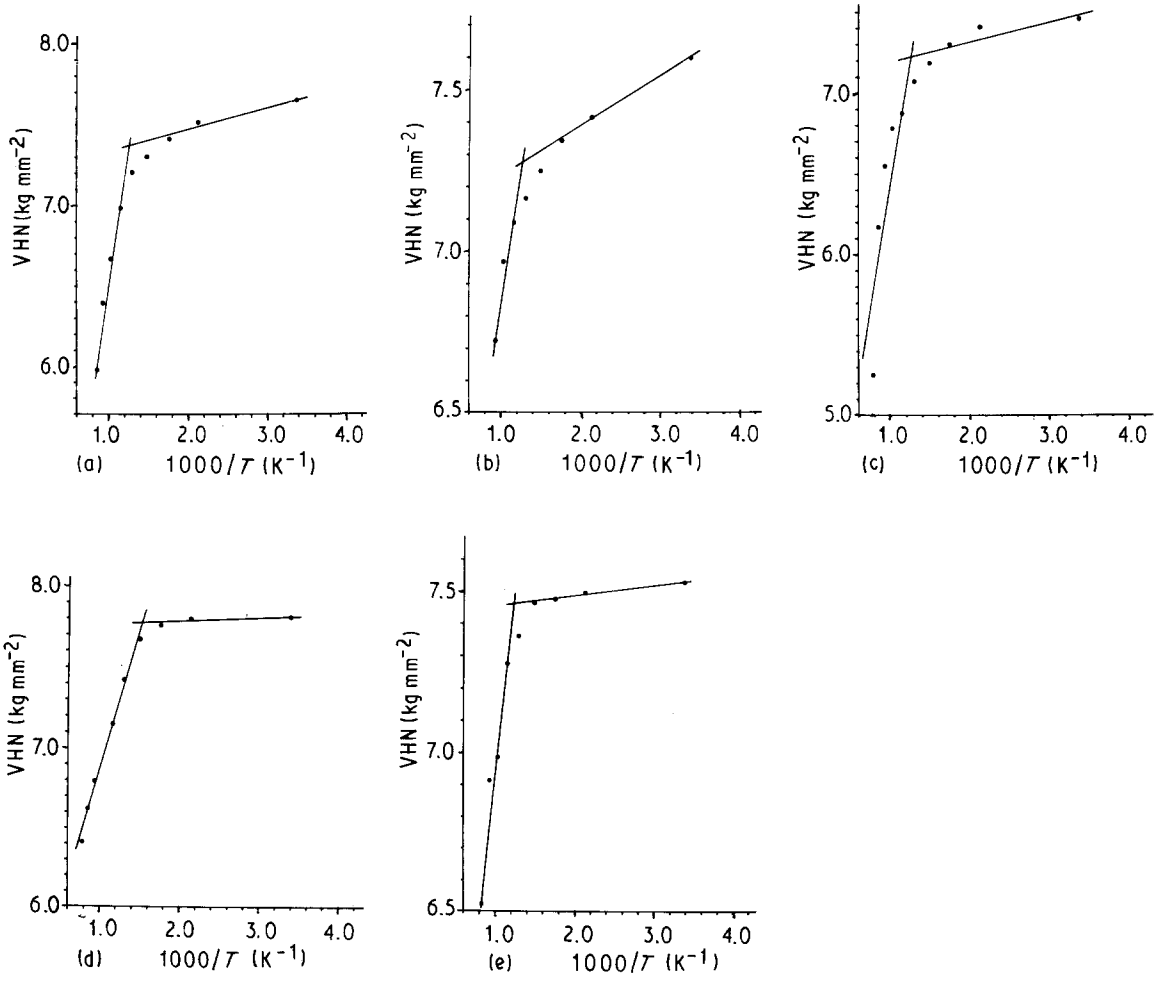

Figure 19 Graphs showing the data from Fig. 18 transformed to show how the activation energy for the deformation process changes: (a) conventional RBSC, (b) RBSC – 15 vol % ZrC, (c) RBSC – 15 vol % TiC, (d) RBSC – 15 vol % B_4C, and (e) RBSC – 15 vol % TiB_2. The line segments were fitted using the method of least squares.

TABLE V Temperature-variant hardness parameters for the novel reaction-bonded materials. The hardness values are for an indentation load of 4.905 N. The activation energy values, Q, were obtained by linear regression on the data. Typical values for the errors in the mean hardness values are $\pm$ 2 GPa (this value is plus or minus two standard errors in the mean, $\pm 2\sigma/n^{1/2}$)

Material	$H_{25\,°C}$ (GPa)	$H_{800\,°C}$ (GPa)	T_{Trans} (K)	Q_{LT} (kJ mol^{-1})	Q_{HT} (kJ mol^{-1})
"REFEL" RBSC	20.6	5.9	840	13.3	202
RBSC – 15 vol % ZrC	19.6	7.8	830	11.9	87
RBSC – 15 vol % TiC	17.7	6.9	910	9.3	226
RBSC – 15 vol % B_4C	24.5	8.8	830	1.9	132
RBSC – 15 vol % TiB_2	18.6	9.8	830	2.6	134

TABLE VI Indentation fracture toughness results for the novel reaction-bonded materials (excluding RBSC – 15 vol % TaC). Each result is the average of five indentation at four loads: 9.81, 24.53, 49.05 and 98.07 N. The expression used to calculate the values is that of Anstis *et al.* [25]. The error is given as $\pm 2\sigma/n^{1/2}$ and is the error in the data. In addition to this error, there is the error associated with calibration constant of the expression

Material	K_{Ic} (MPa m$^{1/2}$)
"REFEL" RBSC	4.0 $\pm$ 0.42
RBSC – 15 vol % ZrC	2.8 $\pm$ 0.28
RBSC – 15 vol % TiC	2.6 $\pm$ 0.18
RBSC – 15 vol % B_4C	2.5 $\pm$ 0.13
RBSC – 15 vol % TiB_2	3.5 $\pm$ 0.38

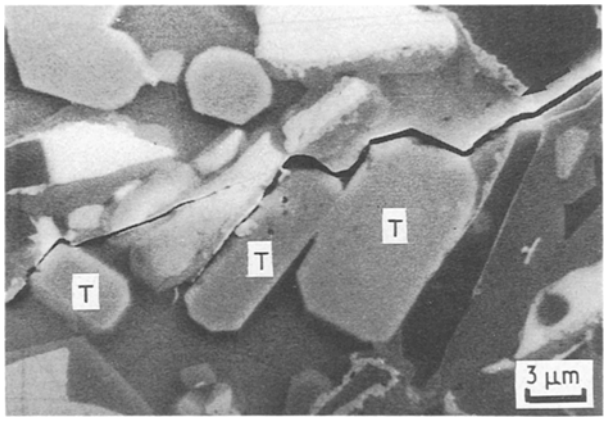

Figure 20 Secondary electron SEM image of the RBSC – 15 vol % TiB_2 pellet showing the deviation of a crack from a Vickers microhardness indentation around three TiB_2 particles (T). The arrow indicates the direction of crack propagation.

temperature (HT) deformation regimes. The 4.905 N hardness values at 25 and 800 °C are also given.

In general, the data for the various materials are disappointingly similar, though perhaps this is understandable because SiC is the dominant phase in all the materials and the silicides formed have similar melting points. The low-temperature deformation mode has a very low thermal activation energy and is presumed to comprise stress-activated plasticity and fracture. Above the transition temperature, which corresponds to about 0.28 of the absolute melting point of silicon carbide and 0.5 of that of silicon, the activation energy is much higher and is probably indicative of temperature-activated dislocation motion in the SiC and possibly even faster creep and creep-related processes occurring in the (lower melting point) silicon and silicide materials. To investigate this high activation energy regime fully, the variation of hardness with time at constant temperature needs to be studied.

3.4.3. Indentation fracture toughness measurements

To make a rapid assessment of the fracture behaviour of the newly fabricated materials, indentation fracture toughness (IFT) tests were performed. These tests also enabled any preferred fracture paths through the microstructure to be identified. The cracks used for the IFT measurements were the traces of what were presumed to be median/radial cracks which propagated from the corners of high load (in this case 9.81–98.1 N) Vickers indentations (serial sectioning was not performed to check the validity of the crack morphology assumption). To obtain values of K_c, the IFT expression of Anstis *et al.* [27] was used

$$K_c = (0.016 \pm 0.004)\left(\frac{E}{H}\right)^{0.5}\left(\frac{P}{c^{1.5}}\right) \quad (7)$$

The results are given in Table VI. There is very little difference between the materials and they have overlapping error ranges. Decreasing the silicon carbide content reduces the measured toughness, silicon having a lower toughness than SiC. The one conclusion which can be drawn is that the new materials are at least as brittle as conventional RBSC (e.g. "REFEL"). No obvious toughening was detected in the RBSC–TiB_2 material as might have been expected if microcrack arrays were generated ahead of the crack fronts. A possible contributory factor to this brittleness is the easy cleavage of many of the silicide phases formed during the silicon infiltration process.

Analysis of the crack paths around indentations did not reveal any obviously preferred paths (unlike Ness [28] who reported that the Si:SiC boundaries were preferred). However, in the case of the RBSC–TiB_2 material, some cracks were observed to deflect quite sharply around the titanium diboride particles (Fig. 20).

4. Conclusion

We have successfully introduced a range of refractory carbides and titanium diboride into the powder mixture used for preparing reaction-bonded silicon carbide. In most cases the reaction-bonding process was not significantly disrupted and near-net-shaped pellets were formed.

However, in the case of the carbides, the simple mixture of phases intended was not obtained but

reaction between the added carbide and liquid silicon to form the metal disilicide and silicon carbide was found to have occurred. The original SiC grit seems to take no part in any reaction except to act as a site for heterogeneous deposition of new silicon carbide formed during the reactions.

Generally, the kinetics of the reaction-bonding process appear to be much faster than those of the metal carbide–silicon reaction. In most cases, this allows a strongly bonded SiC framework to be formed before metal silicide precipitation occurs. This is a key aspect in the retention of the shape of the green compact.

Prediction of the reactions using available thermochemical data was not possible because of the large errors associated with the values and their closeness to zero. The silicides of tantalum, titanium and zirconium have a higher melting point than silicon and thus might be used as a substitute for silicon in RBSC if the reaction can be sufficiently well controlled and the presence of the silicon–silicide eutectic avoided.

TiB_2 did not show any detectable reaction, although it was apparently wetted by liquid silicon. The question of what allows wetting in such circumstances was not addressed.

The mechanical properties, as measured by microhardness, high-temperature microhardness and indentation fracture toughness, of the mixed-phase materials did not show any significant improvement over conventional RBSC. This is partly due to the hardness being dominated by the SiC framework and partly due to brittle silicides replacing some of the SiC. In the case of the RBSC–TiB_2 material, cracks were observed to deflect around the TiB_2 particle–matrix boundaries rather than propagating through the particles. Refining these materials either to induce microcracking or to deflect cracks passing through the mixed-phase microstructure (e.g. by the use of aligned eutectics) is an obvious area for future development.

Finally, it might be possible through very careful control of the composition of the initial compact to produce a material in which all the silicon is replaced by a more refractory silicide, e.g. $TiSi_2$, giving the resultant material improved high-temperature performance.

Acknowledgements

The authors thank Professor R. N. Parkins for the provision of laboratory facilities at the University of Newcastle upon Tyne. This research was performed as part of a CASE programme funded by SERC and sponsored by UKAEA Springfields. The authors also thank Dr Ian Higgins and Mr Peter Kennedy, UKAEA, Springfields, for assistance in the preparation of materials and the use of fabrication facilities.

References

1. P. POPPER, in "Special Ceramics" (Heywood Press, London, 1960) p. 209.
2. P. KENNEDY, in "Non-Oxide Technical and Engineering Ceramics", edited by S. Hampshire (Elsevier Applied Science, London, 1986) p. 301.
3. G. R. SAWYER and T. F. PAGE, *J. Mater. Sci.* **13** (1978) 885.
4. J. N. NESS and T. F. PAGE, *ibid.* **21** (1986) 1377.
5. C. W. FORREST, P. KENNEDY and J. V. SHENNAN, in "Special Ceramics 5", edited by P. Popper (British Ceramic Research Association, Stoke-on-Trent, 1972) p. 99.
6. M. H. LEWIS, G. LENG-WARD and C. JASPER, in "Proceedings of the 1st International Conference on Ceramic Powder Processing Science", edited by G. L. Messing, E. R. Fuller and H. Hausner (American Ceramic Society, Westerville, OH, 1988) p. 1019.
7. K. NEGITA, *J. Amer. Ceram. Soc.* **69** (1986) C308.
8. D. MAGLEY, R. A. WINHOLTZ and K. T. FABER, *ibid.* **73** (1990) 1641.
9. A. J. WHITEHEAD, T. F. PAGE and I. HIGGINS, *Ceram. Engng Sci. Proc.* **10** (1989) 1108.
10. M. G. S. NAYLOR, PhD thesis, University of Cambridge, UK (1981).
11. M. HANSEN, "Constitution of Binary Alloys", 2nd Edn (McGraw-Hill, London, 1958).
12. S. PROCHAZKA, in "Proceedings of the 3rd International Conference on Silicon Carbide", Miami, 17–20 September 1973, edited by R. C. Marshall, J. W. Faust Jr, and C. E. Ryan (University of South Carolina Press, Columbia, SC) p. 394.
13. N. W. JEPPS and T. F. PAGE, *J. Micros.* **124** (1981) 227.
14. R. I. SCACE and G. A. SLACK, *J. Chem. Phys.* **30** (1959) 1551.
15. P. KENNEDY, private communication (1987).
16. A. M. STONEHAM and P. W. TASKER, "Designing Interfaces for Technological Applications", edited by S. D. Peteves (Elsevier Applied Science, London, 1989) p. 217.
17. O. KUBASCHEWSKI and C. B. ALCOCK, "Metallurgical Thermochemistry", 5th Edn (Pergamon Press, Oxford, 1979) p. 267.
18. JANAF (Joint Army, Navy, Air Force) Thermochemical Tables (National Bureau of Standards, Washington, DC, 1971).
19. D. A. ROBINS and I. JENKINS, *Acta Metall.* **3** (1955) 598.
20. S. G. DAVIS, D. F. APTHROP and A. W. SEARCY, *J. Chem. Phys.* **34** (1961) 659.
21. C. E. MEYERS and A. W. SEARCY, *J. Amer. Chem. Soc.* **79** (1957) 526.
22. P. M. SARGENT, PhD thesis, University of Cambridge, UK (1979).
23. S. J. BULL, T. F. PAGE and E. H. YOFFE, *Phil. Mag. Lett.* **59** (1989) 281.
24. P. SCHWARZKOPF and R. KIEFFER, "Refractory Hard Metals: Borides, Carbides, Nitrides and Silicides" (Macmillan, New York, 1953) p. 328.
25. A. G. ATKINS, A. SILVÉRO and D. TABOR, *J. Inst. Metals* **94** (1966) 369.
26. J. A. YEOMANS, PhD thesis, University of Cambridge, UK (1986).
27. G. R. ANSTIS, P. CHANTIKUL, B. R. LAWN and D. B. MARSHALL, *J. Amer. Ceram. Soc.* **64** (1981) 533.
28. J. N. NESS, PhD thesis, University of Cambridge, UK (1985).

Received 19 April
and accepted 1 May 1991